TUDelft

Delft University of Technology

Electrical cross talk of a frequency division multiplexing readout for a transition edge sensor bolometer array

Wang, Q.; Khosropanah, P.; Van Der Kuur, J.; De Lange, G.; Ridder, M. L.; Ilyas, S.; Van Der Linden, A. J.; Van Der Tak, F.; Gao, J. R.; More Authors

Important note
To cite this publication, please use the final published version (if applicable).
Please check the document version above.

Q. Wang, P. Khosropanah, J. van der Kuur, G. de Lange, ⓘ M. D. Audley, A. Aminaei, R. Hijmering, ⓘ M. L. Ridder, S. Ilyas, A. J. van der Linden, ⓘ M. P. Bruijn, F. van der Tak, and J. R. Gao

Review of Scientific Instruments

AIP Publishing

Electrical cross talk of a frequency division multiplexing readout for a transition edge sensor bolometer array (EP)

View Online   Export Citation   CrossMark

Q. Wang,[1,2,a] (ID) P. Khosropanah,[3] J. van der Kuur,[1] G. de Lange,[1] M. D. Audley,[1] (ID) A. Aminaei,[3] R. Hijmering,[3]
M. L. Ridder,[3] (ID) S. Ilyas,[3] A. J. van der Linden,[3] M. P. Bruijn,[3] (ID) F. van der Tak,[1,2] and J. R. Gao[3,4]

AFFILIATIONS

[1] SRON Netherlands Institute for Space Research, 9700 AV Groningen, The Netherlands
[2] Kapteyn Astronomical Institute, University of Groningen, 9747 AD Groningen, The Netherlands
[3] SRON Netherlands Institute for Space Research, 3584 CA Utrecht, The Netherlands
[4] Optics Group, Department of Imaging Physics, Delft University of Technology, 2628 CJ Delft, The Netherlands

[a] Author to whom correspondence should be addressed: Q.Wang@sron.nl

ABSTRACT

We have characterized and mapped the electrical cross talk (ECT) of a frequency division multiplexing (FDM) system with a transition edge sensor (TES) bolometer array, which is intended for space applications. By adding a small modulation at 120 Hz to the AC bias voltage of one bolometer and measuring the cross talk response in the current noise spectra of the others simultaneously, we have for the first time mapped the ECT level of 61 pixels with a nominal frequency spacing of 32 kHz in a 61× 61 matrix and a carrier frequency ranging from 1 MHz to 4 MHz. We find that about 94% of the pixels show an ECT level of less than 0.4%. Only the adjacent pixels reach this level, and the ECT for the rest of the pixels is less than 0.1%. We also observe higher ECT levels, up to 10%, between some of the pixels, which have bundled long, parallel coplanar wires connecting TES bolometers to inductor–capacitor filters. In this case, the high mutual inductances dominate. To mitigate this source of ECT, the coplanar wires should be replaced by microstrip wires in the array. Our study suggests that an FDM system can have a relatively low ECT level, e.g., around 0.4% if the frequency spacing is 30 kHz. Our results successfully demonstrate a low electrical cross talk for a space FDM technology.

Published under license by AIP Publishing. https://doi.org/10.1063/5.0032929

I. INTRODUCTION

Direct detection of the cosmic radiation that contains abundant information about the universe is an important way to address fundamental astronomical questions such as the history of the universe and the origins of galaxies, stars, and planets.[1,2] Cosmic radiation covers the full electromagnetic (EM) spectrum, ranging from the radio, the microwave, the sub-mm, and the far-infrared to gamma- and x-rays. The Transition Edge Sensor (TES) is one of the most promising direct detectors because of its high sensitivity and its wideband response to EM radiation. TES based receiver instruments have been widely used for ground-based telescopes and are also candidates for future space telescopes. TES bolometers operating in the sub-mm and far-IR range approach the photon noise limit, in which the detection performance is limited by fluctuations in the arrival rate of photons at the detector instead of the intrinsic noise

of the detectors. Consequently, increasing the number of detectors can enable higher mapping speeds, as well as covering a large field of view. Large TES arrays with thousands of pixels are needed for future ground and spaceborne telescopes.[3–5] A key challenge in realizing such large arrays has been multiplexing the signals between the detectors on the cold stage at the extremely low cryogenic temperature of ≤100 mK and the electronics at room temperature. Multiplexing limits the number of cold wires and, thus, minimizes the heat load on the cold stage, which is particularly vital for space telescopes, where the cooling power is limited by the available electrical power and the restrictions on the total mass.

Frequency division multiplexing (FDM) is one of the readout systems used for multi-pixel readout[6] of TES arrays. The other popular readout technology is time division multiplexing (TDM).[7,8] In an FDM readout system, the detectors are in series

with inductor–capacitor (LC) filters and are AC biased simultaneously, where the bias frequencies are the resonance frequencies of their corresponding LC filters.[9] The FDM system has several advantages; for example, there is no noise penalty with the increasing number of detectors per readout channel, the LC filters are passive elements with no power dissipation, and each detector bias can be adjusted independently so that all the detectors can be biased optimally, mitigating the effects of detector non-uniformity, e.g., the superconducting critical temperature (T_c) across the array.

FDM readout systems are being used in a number of instruments for ground-based telescopes for detecting cosmic microwave background (CMB) and sub-mm wavelength radiations, such as the Atacama pathfinder experiment Sunyaev-Zel'dovich (APEX-SZ),[10] the South Pole Telescope (SPT),[11] and the Polarization of Background Radiation (POLARBEAR).[12] They are also being considered for balloon-borne mission Large-Scale Polarization Explorer (LSPE)[13,14] and future spaceborne instruments such as SPace Infrared telescope for Cosmology and Astrophysics/SpicA FAR infrared Instruments (SPICA/SAFARI),[15,16] Advanced Telescope for High ENergy Astrophysics/X-ray Integral Field Unit (ATHENA/X-IFU),[17,18] and Lite satellite for the studies of B-mode polarization and Inflation from cosmic background Radiation Detection (Lite-Bird).[19] Usually, fewer readout channels are available in spaceborne instruments than in ground-based ones. This means that the number of pixels per readout channel (i.e., multiplexing factor) is higher, which leads to a narrower frequency spacing between two neighboring resonators and makes it more difficult to keep the electrical cross talk (ECT) level low.

The ECT is defined as the undesired signals that a detector receives from the electrical circuits instead of the signal from the sky or an optical source in the lab. A high ECT can induce errors in the detected signal, decrease the dynamic range, and even destabilize the detector to impede the multiplexing.

It is, therefore, important to characterize and understand the ECT across an array using any new FDM readout system. However, few experimental studies are found in the literature. An ECT study on a TES array with an FDM readout system with carrier frequencies between 350 kHz and 850 kHz and a frequency spacing of 75 kHz has reported a maximum ECT level of 0.4%, where one TES was excited by LED light and responses of five dark pixels were measured.[6] If two systems have the same capacitance and same frequency spacing, the higher carrier frequency means a lower inductance, which can lead to a higher carrier leakage. A preliminary measurement was also reported that characterized the ECT by introducing x-ray pulses to TES micro-calorimeters, reading the other five pixels with a frequency spacing of at least 200 kHz.[20] The importance of the wiring to TES bolometers on the array chip has been simulated to relate high mutual inductance to the ECT in our lab,[21] but no dedicated experiments on the effect of the wiring have been reported so far.

In this paper, we experimentally study the ECT in our FDM system that reads out 61 TES pixels with a nominal frequency separation of 32 kHz. We present a method to measure and map the ECT among all the pixels connected, identify the major sources of the ECT, and discuss ways to improve them.

II. FDM WITH BASEBAND FEEDBACK

Figure 1 shows an electrical schematic diagram of the FDM readout with baseband feedback (BBFB) that we used for the ECT study. TES bolometers are connected in series with narrow
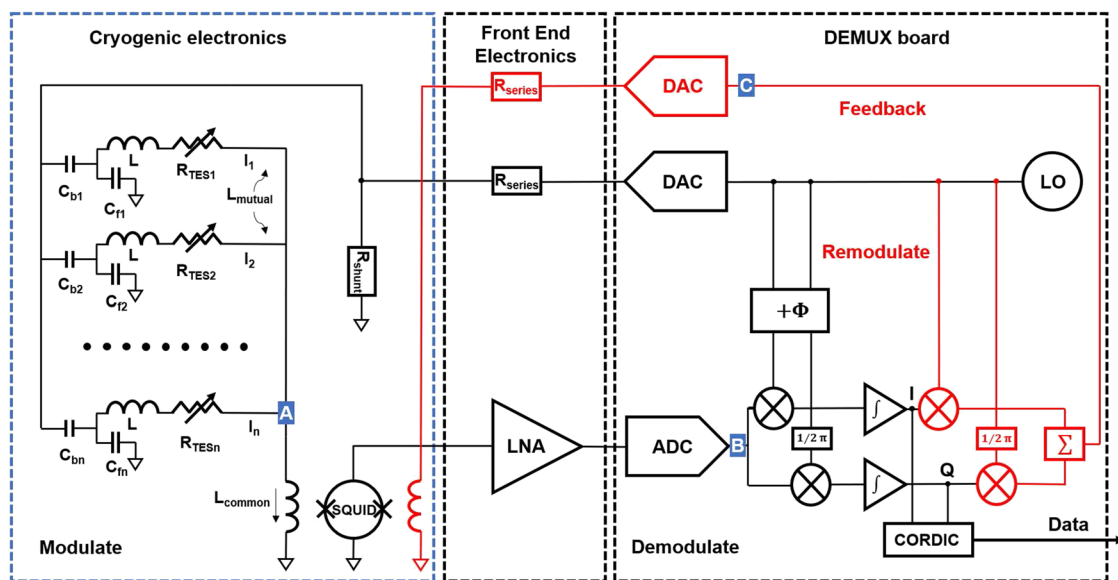
FIG. 1. FDM readout electrical schematic with baseband feedback (BBFB). The DAC provides AC bias voltages in the frequencies corresponding to the resonance frequencies of LC filters for the TES bolometers. The currents through TES bolometers are summed at the input coil of the SQUID amplifier, indicated by point A. The SQUID amplifies the amplitude-modulated signals at its output. After further amplification by the room-temperature LNA, the signal (at point B) is demodulated to I and Q information, then collected by using a CORDIC (COordinate Rotation DIgital Computer). In the feedback process, these signals are re-modulated and applied to the feedback coil (at point C) of the SQUID with appropriate phase shifts to cancel out the SQUID output.

TABLE I. FDM readout system parameters.

TES normal state resistance: 200 mΩ	SQUID input inductance: 1.5 nH
TES critical temperature: 110 mK	Inductance of LC filters: 3 μH
TES Ti/Au bolometer size: 50×50 μm^2	Capacitance of LC filters: 1 nF–9 nF
TES Ta absorber size: 100×100 μm^2	Carrier frequency f_0: 1 MHz–4 MHz
TES Si_3N_4 legs volume: $400 \times 2 \times 0.25$ μm^3	Frequency spacing Δf: 32 ± 3 kHz
Designed NEP level: 0.7 $aW/\sqrt{Hz}$	$\Delta f/f_0$: 0.08–0.32
SQUID mutual inductance: 27 $\mu A/\Phi_0$	Readout current noise: 20 $pA/\sqrt{Hz}$

bandpass cryogenic LC filters.[22] The room-temperature demultiplexer (DEMUX) electronics generates a comb of tones (i.e., carriers) with frequencies ranging from 1 MHz to 4 MHz. Each of these tones is tuned to match the resonance frequency of one of the LC filters and provides an AC voltage bias to the corresponding TES. The LC filters also reject the wideband Johnson noise in the circuit. The TES currents are summed at the input coil of a superconducting quantum interference device (SQUID) amplifier. The signal at the output of the SQUID amplifier is essentially an amplitude-modulated version of the AC bias signal with a phase shift due to the electronics and wire harness. After further amplification by using a low noise amplifier (LNA) at room temperature, the output signal is demodulated to recover the bolometer electrical signals or optical signals if there is a sky source. These signals are then re-modulated using the same carrier tones with appropriate phase shifts and added to cancel out the SQUID output when applied to the feedback coil of the SQUID. This scheme is known as BBFB. A common shunt resistor (R_{shunt}) of 100 mΩ is used to provide a bias voltage for all the bolometers. The cryogenic electronics, including TES bolometers, LC filters, and SQUID, are at a temperature below the critical temperature (T_c) of a TES, typically at the base temperature of a cooler, while both the front-end electronics and DEMUX board are at room temperature.

All the measurements described in this paper are performed in an environment, intended to be dark, i.e., with no designed optical signals to the bolometers. However, there might be some influence of stray light that contributes to photon noise, which could increase the noise level in the measured noise spectrum. In this paper, the signals we use for the electrical cross talk study are well above the detector noise, so the presence of stray light has negligible influence on our conclusions. The signals in the TES array are only electrical, AC bias tones from the DAC (digital-to-analog) device in an SRON homemade DEMUX board. All the signals are added in the summing point and then amplified by the SQUID. We demodulate the output signal to I and Q parameters to analyze and re-modulate them with a delayed carrier for the BBFB.[23] We expect the ECT to happen mainly in the cold part of the FDM readout system. The ECT can be caused by a number of mechanisms,[6] but here, we focus on the most important sources to introduce the ECT in an FDM system.

The ECT described in this paper can be attributed in general to a combination of carrier leakage, mutual inductance (L_{mutual}), and common inductance (L_{common}). Carrier leakage occurs when part of the current at the specific frequency that is intended for one detector leaks out to the other detectors because the LC filters are not perfect. Mutual inductance and common inductance are indicated in the cryogenic electronic part of Fig. 1. The mutual inductance is the magnetic coupling between two TES bias circuit branches,[21] which

can happen not only between the wires but also between the coils in the LC filters. The common inductance is the total sum of the inductance after the summing point, including the inductance of the input coil of the SQUID. The presence of common inductance makes the resonance frequencies of the circuit slightly different than those of the LC filters, which effectively means that the detectors are biased slightly off-resonance. Table I contains some of the main parameters of our FDM readout system.

III. EXPERIMENTAL SETUP

Figure 2 shows the cold electronics part of our FDM setup, designed as a prototype of the SAFARI instrument on SPICA.[24] It contains a 176-pixel TES array chip in between two LC chips with 88 resonators each and a SQUID amplifier as indicated. These are mounted inside a copper bracket, which is designed to be light-tight. It also holds a Helmholtz coil to eliminate the background magnetic field (not visible in Fig. 2). A Janis adiabatic demagnetization refrigerator (ADR)[25] is used to cool down the bracket. The lowest temperature it can reach is 50 mK, but with a relatively short operating duration. When it is operated at 90 mK, the ADR can run
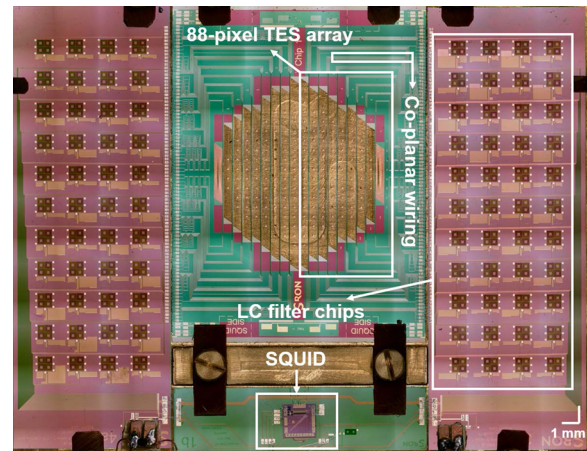
FIG. 2. Photo of the cold electronics part of the FDM readout system with the TES array chip in the middle, LC filter chips on the two sides, and the SQUID chip at the bottom. The array contains 176 pixels. The half array of 88 pixels, 84 bolometers, and four resistors is connected to simplify our measurement and analysis. The LC filters connect with the TES array via microstrip lines in the LC filter chip, bonding wires, long coplanar wiring, and wires around TESs in the TES array chip. All the chips are mounted inside a light-tight copper bracket at 90 mK, which is not shown in the figure.

for more than 10 h, stabilized with a temperature variation of less than 0.01 mK. Thus, most of our measurements were performed at 90 mK.

In the 176-pixel bolometer array, each bolometer has a TiAu TES with an area of $50 \times 50\,\mu m^2$ and a $100 \times 100\,\mu m^2$ thin Ta optical absorber. Both are defined on a Si_3N_4 membrane island, which connects with the Si substrate at the bath temperature through four long (400 μm), narrow (2 μm), and thin (0.25 μm) Si_3N_4 legs,[24] which determine the thermal conductance between the TES and the thermal bath. The bolometers have a T_c of about 110 mK. The designed Noise Equivalent Power (NEP) of the TESs is 0.7 $aW/\sqrt{Hz}$. With a similar TES structure, we can provide an ultra-low NEP of 0.2 $aW/\sqrt{Hz}$.[26] It is worth mentioning that eight of the pixels in the array are just simple resistors for calibration purposes.

The LC filters consist of low-loss dielectric capacitors and inductors and have a Q-factor of 10 000 or higher at 90 mK. The inductance of all the inductors is designed to be 3 μH, while the capacitance of the capacitors varies from 1 nF to 9 nF in order to adjust the frequency for each pixel, targeting an equal frequency spacing of 16 kHz. In reality, the total capacitance of an LC filter is a combination of the capacitance of a bias capacitor (e.g., C_b) and that of the capacitor in the filter (e.g., C_f), as illustrated in Fig. 1. The

ratio between the filter and bias capacitances is 10 nominally, and each pair acts as a voltage divider in the bias circuit. The bias frequency ranges from 1 MHz to 4 MHz for the full array using two LC chips. To simplify the experiment, we choose to connect only half of the TES array to one LC filter chip (88 pixels connected) so that the frequency spacing is doubled (32 ± 3 kHz). Aluminum wire bonds are used for connecting the chips in the mK stage.

The SQUID amplifier used is a single-stage SQUID developed at the National Metrology Institute in Germany (PTB), and the readout current noise of the SQUID-LNA chain is 20 $pA/\sqrt{Hz}$.[27,28]

Before starting a multiplexing readout measurement, we use a network analyzer (NWA) to measure the resonance frequencies of all the LC filters. Eventually, we selected 61 TES pixels that are connected to LC filters with a Q-factor higher than 10 000 for ECT measurements. Fine tuning of a resonance frequency is done by looking for a peak in the frequency scan when a TES is operated in the superconducting state. Then, we fix the frequency and choose an appropriate phase delay for remodulation that allows us to close the BBFB loop stably. This process is called locking a pixel.

When all 61 TES pixels are simultaneously locked in their superconducting to normal transition, we take the current–voltage (IV) curve and the current noise spectrum of each pixel for a general health check of the FDM readout system and then start to
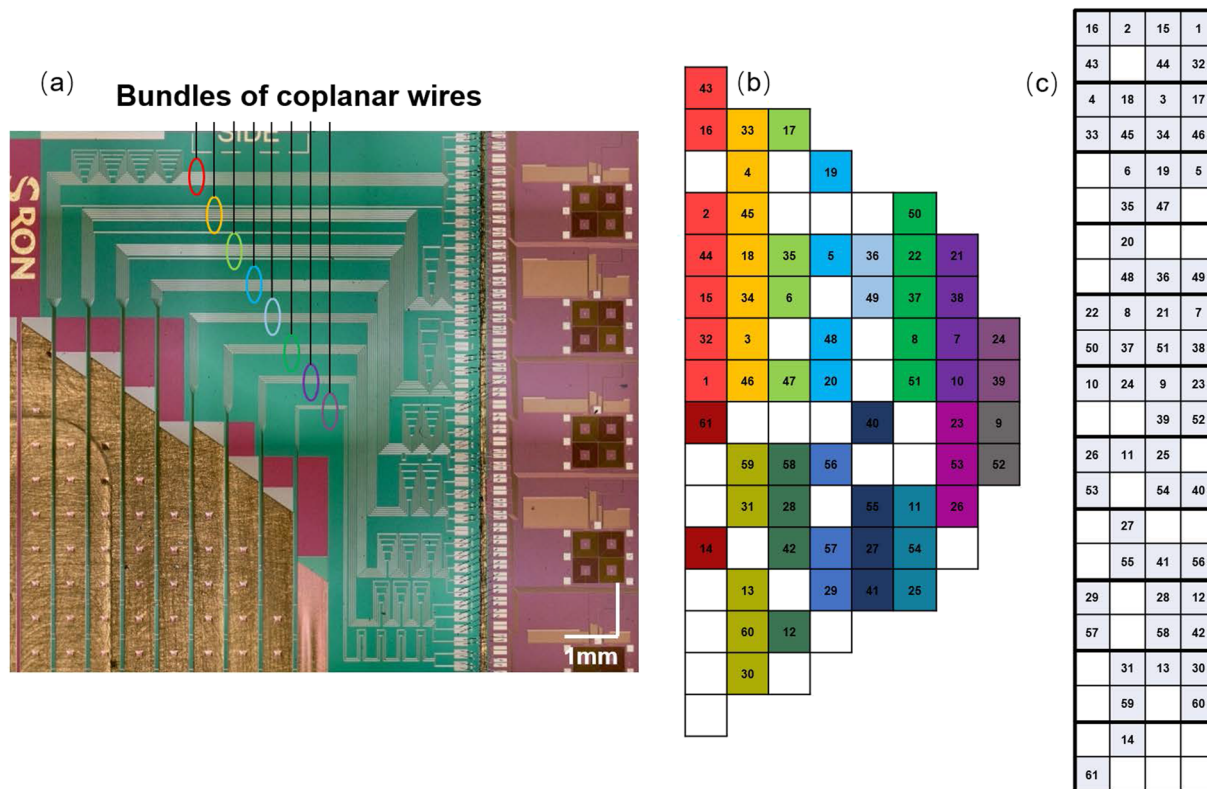
FIG. 3. (a) Zoomed photo of long, parallel coplanar wires in a number of bundles to connect TES bolometers to the bond pads. The coplanar wires are several centimeters long and have additional meander structures to adjust all the wires in the same bundle to have the same length. Different bundles of wires are circled in different colors. (b) Map of the connected pixels in the half array; pixels sharing the same bundle for the wiring are indicated by backgrounds of the same colors. (c) Map of the LC filters with the numbers corresponding to those of the pixels in the array in (b).

characterize the ECT. Figure 3(a) shows an enlarged picture of the wiring on the TES array chip and the LC filter chip, where the Nb coplanar wiring is defined on the TES array and is electrically connected to the LC filter chip by wire bonds. On the LC filter chip, the wiring is made of microstrip lines, which are the superconducting Nb wires, sandwiched with an SiO_2 insulating layer. To decrease the mutual inductance between the coils in the LC filters, the TES pixel neighbors in the frequency space are not the physical neighbors, as shown in Fig. 3(c). Meander structures in the coplanar wires are introduced to compensate for different wiring lengths to fix the frequency spacing. Those long coplanar wires that are bundled in parallel and marked by the same color in Fig. 3(b) cause potential ECT among the corresponding pixels due to the mutual inductance of the closely packed wire loops.

IV. FORMS OF ELECTRICAL CROSS TALK

A. Carrier leakage

Due to carrier leakage, parts of the bias currents intended for other detectors leak into each detector. These are off-resonance bias currents with various frequencies that add up quadratically and can potentially destabilize the detector biasing when the total sum becomes comparable to the detector's own on-resonance bias current. The carrier leakage current ratio between the on-resonance pixel and a neighboring pixel approximately equals to $\left| \frac{R_{TES}^2}{(2\Delta\omega L)^2} \right|$, where $\Delta\omega = 2\pi\Delta f$, Δf is the frequency separation between two adjacent pixels, L is the inductance of the LC filters and equals $3 \pm 0.1\,\mu H$, and R_{TES} is the resistance of the TES at its operating point.[6] Our bolometers are usually biased in the transition with the resistance at 30% of the normal state resistance R_n, which is 200 mΩ. The relative carrier leakage current is calculated to be 0.25% if the frequency separation is 32 kHz. This number increases to 1.0% if the frequency spacing decreases to 16 kHz, which is the case if the full array is connected. This carrier leakage current dependence on frequency spacing has been separately verified with our LT-Spice model of the TES LC resonators. The carrier leakage comes not only from the neighboring pixels but also from the others in the array. To account for all the carrier leakage contributions, we need to consider all the off-resonance pixels by the following equations. The impedance of a TES and its connected LC filter as a unit in Fig. 1 can be expressed as

$$Z_n = \frac{1}{\frac{1}{j2\pi f_n L + R_{TESn}} + j2\pi f_n C_{fn}} + \frac{1}{j2\pi f_n C_{bn}}, \quad (1)$$

where f_n is the resonance frequency of the LC filter, and C_{fn} and C_{bn} are the capacitances of the capacitor in the LC filter and the bias capacitor, respectively. The leakage current amplitude through the TES and LC filter unit can be written as a unit voltage divided by the impedance Z_n,

$$Y_n = \frac{1}{Z_n}. \quad (2)$$

Then, the leakage current through the TES branch can be seen as the shunt of the total current through the TES and LC filter unit,

$$I_n = Y_n \cdot \frac{1}{\frac{1}{j2\pi f_n L + R_{TESn}} + j2\pi f_n C_{fn}} \cdot \frac{1}{j2\pi f_n L + R_{TESn}}. \quad (3)$$

Figure 4(a) shows the calculated currents in 88 detectors using Eqs. (1)–(3) with the 32 kHz frequency spacing. The frequency span
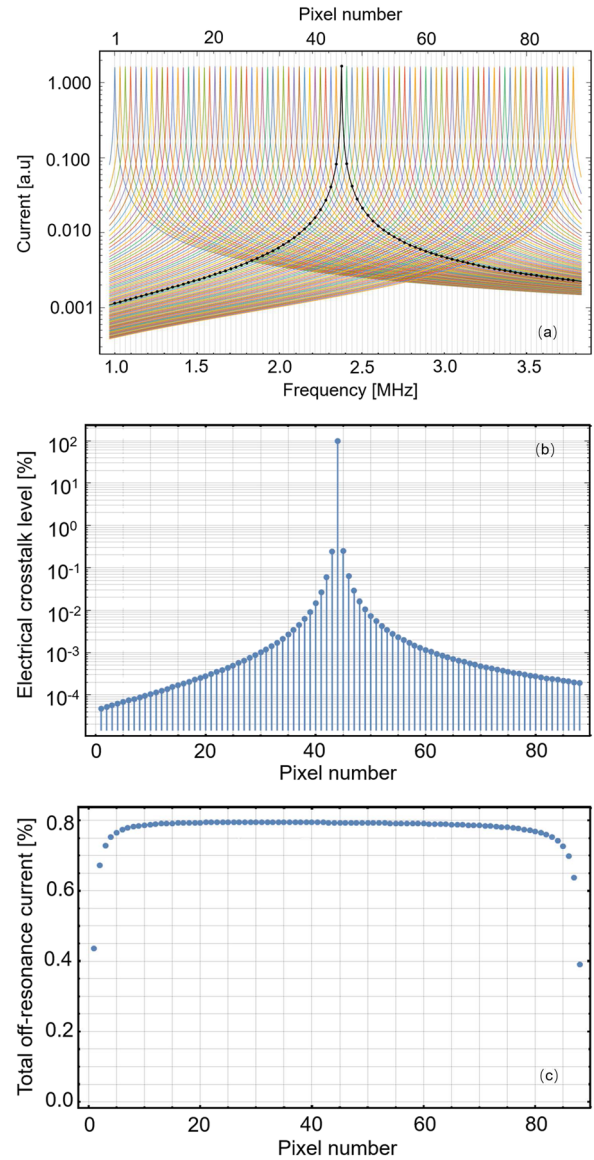
FIG. 4. (a) Simulated currents of 88 TES pixels, biased in the transition with 30% of the normal state resistance, are plotted in colors as a function of frequency. The black curve is the current of pixel 44 in the middle of the frequency span, which has a maximum carrier leakage from neighbors on both sides. (b) The calculated ECT due to carrier leakage from all the other pixels to pixel 44. (c) The ratio of the total off-resonance leakage current to the total bias current for each pixel expressed as a percentage. The first and the last pixel are at the two ends of the frequency span and have the lowest cross talk levels because they have neighbors on only one side in frequency space.

is chosen to be from 1 MHz to 4 MHz, which is similar to our experiment. All the pixels are biased at 30% in their transition. The pixels are numbered sequentially in the frequency span, where pixel 1 is at the lowest frequency and pixel 88 at the highest. Pixel 44, which is in the middle of the frequency span, is chosen to illustrate the carrier leakage current in Fig. 4 because it has the highest number of neigh-

bors on both sides. This leads to a higher carrier leakage than the pixels at the two ends of the frequency span as shown by Fig. 4(c), where the neighbors from only one side contribute. Figure 4(b) shows the calculated ECT of pixel 44 due to carrier leakage, contributed by all the other pixels. ECT from each pixel to pixel 44 in this case is calculated by quadratically dividing the leaking current of this particular pixel by the current of pixel 44 since the leaking current is off-resonance. The highest ECT, which is 0.25%, comes from the nearest neighbors. The total leaked current from all the other pixels to each pixel can be calculated by quadratically adding individual leaked currents; this is ≤0.8% of the total bias current, as shown in Fig. 4(c). The ECT value due to carrier leakage will decrease with increasing frequency spacing and will increase with increasing bias voltage, causing the TES to operate higher in the transition. For example, the ECT level will become 0.69% when a detector is biased at 50% of the normal resistance.

B. Mutual inductance

To bias and readout each bolometer in the array, two superconducting wires are required. They form a current loop through the TES, which consists of the wires connecting the TES through two Si_3N_4 legs, long coplanar wires to further connect bonding pads, bonding wires, and microstrip wires on the LC filter chip, as shown in Fig. 3(a). Because of the mutual inductance between these loops, part of the bias current from one detector couples to the other detectors, causing cross talk. The closer the loops, the higher the mutual inductance between them, while for the ones that are far apart, the coupling is negligible. The mutual inductance contributed by coplanar wiring in the array chip has been simulated previously,[21] where the long coplanar wires that connect TES bolometers to LC filters can introduce a relatively high mutual inductance, which accounts for 59% of the total mutual inductance. It is important to note that in the simulation, the mutual inductance due to LC filters accounts for 31% of the total mutual inductance, but this value is significantly lower in our experiment. This is due to the fact that the LC filter chips have been redesigned here so that the resonators that are neighbors in resonance frequency are not physical neighbors. The same simulation also shows that microstrip wires make a small contribution (1.4%) to the total mutual inductance. Therefore, the mutual inductance that comes from coplanar wires is expected to be the dominant factor in our case.

C. Common inductance

Due to common inductance, the resonance frequencies of the circuit, including TES, LC filter, and SQUID, are slightly different from the frequencies of the LC filter in series with the detectors. Large common inductance forces us to operate the detectors far off-resonance, which enhances the cross talk level, so it is important to keep that as low as possible. The common inductance includes coupled inductance of SQUID feedback coil, inductance from wire bonds, and geometric inductance of the lines.[6,29] In our case, the common inductance is dominated by the input coupling inductance of the SQUID. The common inductance in our setup can be probed by a Network Analyzer (NWA) scan through the feedback line.[24] As shown in Fig. 5, each LC filter appears as a peak and a valley in such a scan. It is known[24] that the frequencies corresponding to the peaks are determined by the sum of the inductance of the LC filters
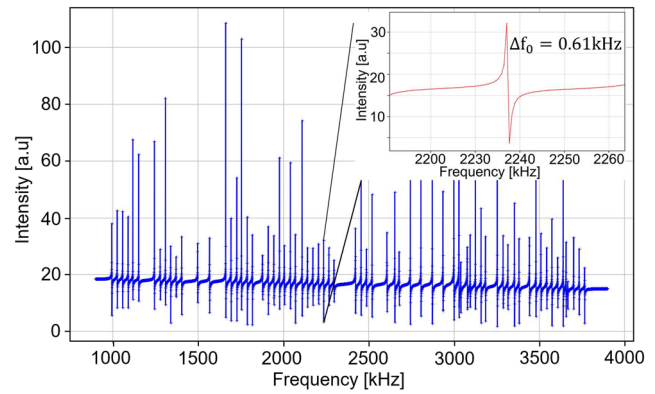
FIG. 5. Network analyzer scan through the feedback line. The inset focuses on the resonance of pixel 29 at f_0 = 2236 kHz, where the frequency difference Δf_0 between the peak and the valley is 0.61 kHz, which corresponds to a common inductance of 1.64 nH.

and the common inductance, while the valleys are the signature of the resonance frequencies of the LC filters only (f_0). The common inductance can then be derived from the following expression:

$$L_{com} = L\left[\left(\frac{f_0}{f_0 - \Delta f_0}\right)^2 - 1\right], \qquad (4)$$

where L is the inductance, f_0 is the resonance frequency of an LC filter, and Δf_0 is the frequency difference between a peak and a valley. Looking closely at f_0 = 2236 kHz (Fig. 5 inset), Δf_0 is 0.61 kHz, with L = 3 μH; using Eq. (4), we find that our setup has a common inductance of only 1.64 nH. In the absence of any common inductance, the resonance frequencies are solely determined by the capacitances and the inductances (LC filters) that are in series with the TES detectors. However, in the presence of a common inductance, the same number of resonators are observed but all the resonance frequencies are slightly shifted. When $L_{com} \ll L$, the frequency shift can be written as $\Delta f_0 \approx 0.5 f_0 L_{com}/L$. When we operate at these resonance frequencies, we are slightly off-resonance in reference to what is defined by the LC filters. This translates to an additional impedance (Z_{com}) in series with the detectors in the same branch circuit, which is $Z_{com} = 4\pi\Delta f_0 L$, and substituting the Δf_0 value mentioned above, it can also be written as $Z_{com} = 2\pi f_0 L_{com}$. If this impedance becomes comparable to the TES resistance at the operating point, it will affect the level of cross talk by increasing the carrier leakage as illustrated by the formula $\left|\frac{R_{TES}^2 + Z_{com}^2}{(2\Delta\omega L)^2}\right|$. The Z_{com} provides a negligible increase in carrier leakage in the low-frequency range due to the low value of Z_{com}. This impedance will become large (about 40 mΩ) at the high end of our bias frequency range. When we bias the high-frequency detectors at 50% transition (about 100 mΩ), the ECT level will increase from 0.69% to 0.79% due to this common impedance. Therefore, even in the highest bias frequency, the influence of common inductance is very small. In addition, the common inductance will indirectly affect the ECT through the off-resonance and frequency separation argument. The off-resonance due to common inductance in our highest frequency of 3900 kHz is only 1.07 kHz, which means that this largest frequency shift gives 3.3%

shift in frequency with respect to the 32 kHz separation in our case. In summary, the 1.64 nH common inductance will give a negligible influence on the ECT in the operating frequency range of 1 MHz–4 MHz.

V. EXPERIMENTAL RESULTS AND DISCUSSIONS

A. Three-pixel measurement

Our technique for characterizing the ECT is as follows: We choose three bolometers first, pixel 24 in the middle and its two adjacent pixels 23 and 25. First, we bias all three detectors at their usual operating point, 50% in the transition. In our FDM system, it is possible to set a low-frequency amplitude modulation of different kinds on a fraction of the full amplitude of the AC bias signal. This is a powerful tool that can be used for triggering or other diagnostic purposes such as measuring the complex impedance of the detectors.[30] We use this to excite pixel 24 by sine-wave modulating 1% of its bias voltage at a frequency of 120 Hz. We choose 1% because it gives us a sufficiently large signal, well above the noise level but at the same time creates no obvious harmonics that disturb the noise spectra. There is nothing special about the 120 Hz other than being well within the detector response speed and away from the power line frequency of 50 Hz and its harmonics. Since this modulation frequency is much lower than the AC bias frequency (i.e., 1 MHz–4 MHz), the measured ECT is independent of the exact modulation frequency, and any frequency within the detector band serves our purpose. We now record the current noise spectra of these pixels simultaneously. In the absence of the ECT, only the excited pixel is expected to have a peak at 120 Hz in its noise spectrum. If peaks at 120 Hz also appear in the noise spectra of other pixels, it means that part of the modulated bias of the excited pixel also biases other pixels, and the ratio of peaks can be used as a measure of the cross talk. Figure 6(a) shows
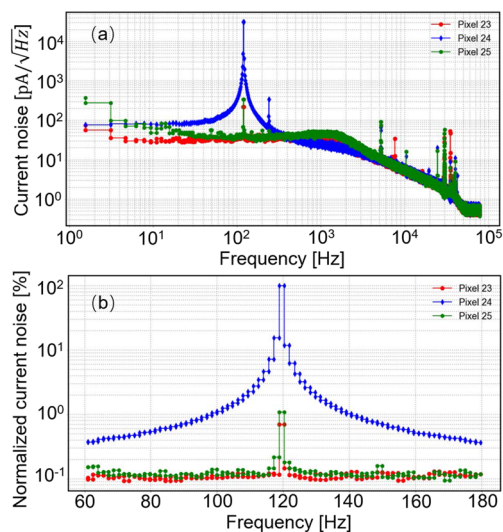

FIG. 6. (a) Current noise spectra of three neighboring pixels, where pixel 24 is excited by 1% modulation at 120 Hz on its AC (MHz) bias voltage. The spectra are recorded simultaneously using the FDM readout. The line at 240 Hz in pixel 24 is a harmonic of the modulation. Some lines beyond 5 kHz are the noise lines due to DEMUX and FEE electronics. (b) The current noise spectra of the three pixels around 120 Hz normalized to the peak at 120 Hz in pixel 24.

the demodulated noise spectra of these three pixels in a frequency span from 1 kHz to 100 kHz, where we will focus on the peaks at 120 Hz. We define the peak at 120 Hz in the spectrum of pixel 24 as the excited peak and in the spectrum of pixel 23 or 25 as the responding peak. The ratio of a responding peak to the excited peak is attributed to the level of ECT between two pixels. Figure 6(b) shows the normalized peaks on a logarithmic scale, where the ECT for pixels 23 and 25 is measured as 0.7% and 1.0%, respectively. The ECT level can be well explained by the carrier leakage simulation, which gives a 0.69% ECT level with detectors biased at 50% in the transition. The higher ECT between pixel 24 and pixel 25 is expected since the frequency space between these two pixels is 30 kHz and slightly less than the frequency spacing between pixel 23 and 24, which is 35 kHz. Furthermore, the operating point of the TES can also influence the ECT, because the cross talk due to carrier leakage decreases as the operating point goes lower in transition. First, our TES bolometers are typically operated in a range of 30%–50% of the resistance transition. When we start with the three-pixel experiment, we bias them at 50% transition. Because of the higher resistance at this bias point, a higher ECT due to carrier leakage is expected. Then, for the measurement with the entire array, ideally we want to bias all our detectors at the 30% transition but we were not able to do so due to the fact that the detectors' response speed was too fast at this bias point and caused oscillations. To avoid this, some of the pixels were biased at 50% transition or higher.

B. 61-Pixel TES array measurement

Now, we extend the method to map the ECT across the TES array. Once all the pixels are biased in the transition and are locked, the FDM system can measure the current noise spectra of all connected pixels in the array simultaneously. Then, we apply the same method as that for the three-pixel measurement to the whole array, going from the first pixel to the last. For each excited pixel, we record the ECT levels in the other 60 pixels and form a 1 × 61 array, shown as one row in Fig. 7. We assign a value of 100% for the excited pixel itself that is marked in black in that row. In this way, we can summarize the ECT level for all 61 pixels to generate the 61 × 61 matrix, as shown in Fig. 7. Pixel 1 corresponds to the lowest frequency of 1 MHz, while pixel 61 corresponds to the highest frequency of 3.9 MHz in this case. The noise level around 120 Hz, which we call the background noise, can influence the accuracy of the measurement, especially for those pixels that are far away from the excited pixel in frequency and show a weak response. Therefore, before calculating the ratio of the peaks, we quadratically subtract the background noise from all the peaks.

We repeat this process by exciting each pixel one by one and reading out the noise of the entire array to map out the ECT as shown in Fig. 7. In each row, the excited pixel number is the same as the row number and marked in black. The levels of the ECT observed in other pixels when this one is excited are illustrated by colors in that row. Similarly, in each column, the responding pixel number is the same as the column number and marked in black. The levels of the ECT observed in this pixel when others are excited are illustrated by colors in that column. About 94% of the squares in the 61 × 61 ECT matrix are blue, meaning that they are below the 0.4% level, suggesting that some of them approach zero. The pixels that are far away from the excited pixel in the frequency space
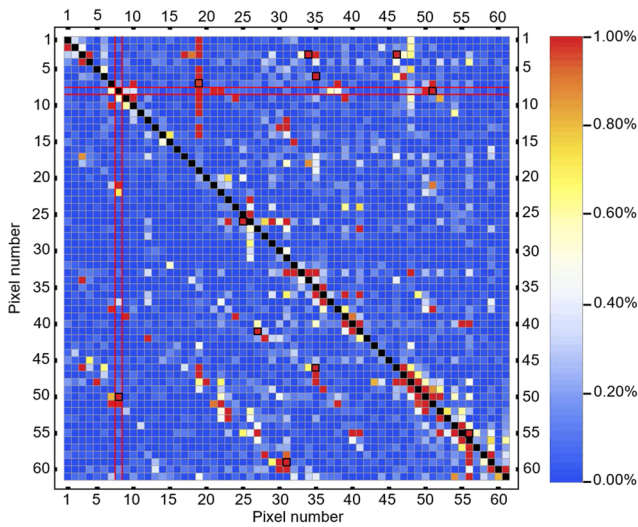
FIG. 7. Electrical cross talk level of 61 pixels out of a TES array readout simultaneously in a multiplexing mode by using an FDM system. In this 61 × 61 matrix, each row presents the cross talk level of the pixels, caused by one of the pixel with black color. The number represents the pixel from 1 to 61, which follows the order of the biasing voltage frequency from 1 MHz to 4 MHz. The level of the cross talk is indicated by color, quantified by the color bar in the figure, where we plot the level only up to 1% for clarity. If the level is above 1%, the color will be the same as that for 1%. We add a black boundary "□" to the filled red square "■" for the points with the ECT higher than 10%. The column presents the cross talk level of the pixels, which contribute the cross talk to the pixel in black. Row 8 and column 8 are marked to stress the comparison in their level distributions.
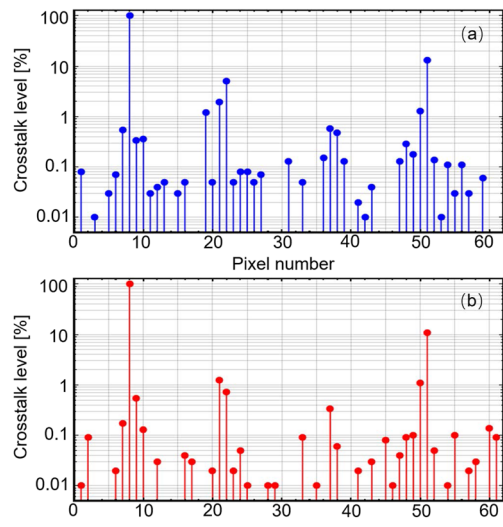
FIG. 8. (a) Measured cross talk level of 61 pixels except for pixel 8, which is used as the excitation. The dataset is the same as row 8 in Fig. 7, but is now plotted numerically. (b) Cross talk level of 61 pixels from column 8 in Fig. 7.

are expected to show a negligibly low cross talk level if the carrier leakage is the dominant mechanism. Those pixels adjacent, for example, to pixel 8 in the matrix have an ECT level around 0.4%. This value can be explained by the overall carrier leakage level in our setup with a nominal frequency spacing of 32 kHz and with TES bolometers biased at 30%–50% in the transition region. A number of high-frequency biased pixels, or the high pixel numbers from 46 to 61, show high ECT levels of 0.4%–1% to their adjacent pixels. We refer to the right bottom corner of the matrix in Fig. 7. This is partly because the cross talk due to the mutual inductance increases with the resonance frequency. Another reason is that the higher the frequency, the larger the frequency shift due to the common inductance, leading to a higher carrier leakage. This can be seen by rewriting Eq. (4) as

$$\Delta f_0 = \frac{f_0\left(\sqrt{\frac{L_{com}}{L} + 1} - 1\right)}{\sqrt{\frac{L_{com}}{L} + 1}}. \tag{5}$$

Since the common inductance is constant, the frequency shift is proportional to the resonance frequency. Therefore, the bolometers with higher bias frequencies, e.g., 3 MHz, will have a larger shift of resonance frequency than those with lower bias frequencies of 1 MHz. In column 19, the high ECT levels that appear between row 1 and 14 are due to pixel 19 that was not biased stably when pixel 1–14 were excited.

In Fig. 8, we focus on pixel 8 and take a closer look at the data in the eighth row and column of the cross talk map. We see that although there are similarities between Figs. 8(a) and 8(b), they are not exactly the same. This means that the ECT caused by pixel 8 to the rest of the array is different from that caused by the rest of the array to pixel 8. This is expected in our system because of the non-uniformity of the TES array and the fact that not all the pixels are biased at the exact same point in the transition. Thus, the bolometers have a different responsivity, and therefore, the ECT map is non-symmetric. In addition, the cross talk due to mutual inductance is proportional to the resonance frequency, which means that the cross talk from a high-frequency pixel to a low-frequency pixel is higher than the other way around. In other words, even if all the bolometers were the same and also operated under the same bias condition, we would not have expected a symmetric ECT map. It is interesting to note that, although some of the pixels have a large frequency separation from the excited one, they show a high level of ECT of 1% or more and together form approximately diagonal patterns across the cross talk map, visible in Fig. 7. For example, there are high levels of ECT between pixels 8, 21, 22, 50, and 51.

The high ECT level is most likely due to the high mutual inductance in the coplanar wires that connect bolometers to LC filters. In our setup, pixels 8, 21, 22, 50, and 51, which appear to have a high level of ECT, make use of long, parallel coplanar wires, which are closely packed in a bundle as circled in Fig. 3(a) and grouped in the same color in Fig. 3(b). To prove this hypothesis, we assume a high ECT level among the bolometers that use the long coplanar wires in a common bundle, but no difference in the amplitude. These pixels are marked in black in a new 61 × 61 matrix in Fig. 9(a). As we can see, these pixels form approximately parallel, diagonal patterns in the matrix. To have a comparison with the measurement, we now overplot Figs. 7 and 9(a), resulting in Fig. 9(b). We find that the parallel, diagonal-lined distribution matches reasonably well with the measured high ECT pixels distributed along or in the vicinity
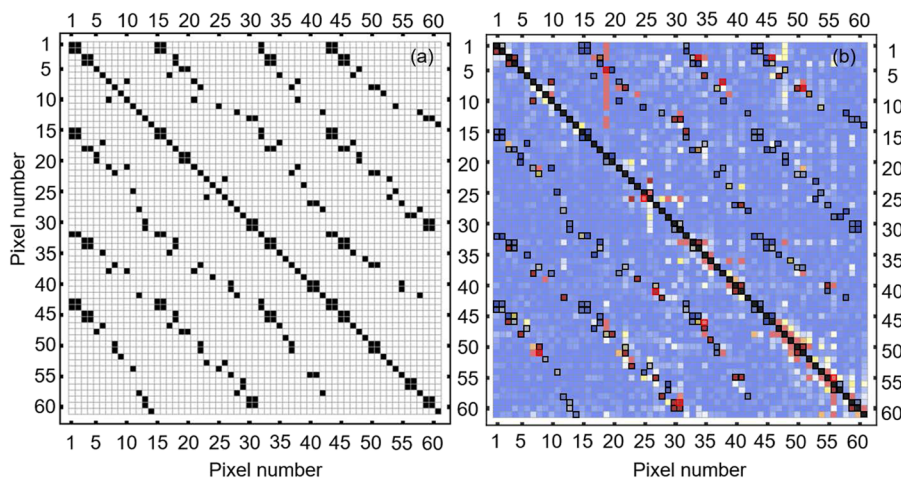
FIG. 9. (a) Pixels (represented by filled squares in black) connected with long, coplanar wires in a bundle, assumed to have a high cross talk due to mutual inductance, are shown on a 61 × 61 matrix; their distribution is characterized by a number of parallel, diagonal lines. (b) The pixels with the high cross talk in (a) are now represented by empty squares with a black boundary "□" and are superimposed with 50% transparency to the measured cross talk matrix from Fig. 7, where the measurement data also show the parallel, diagonal line distribution as in (a). For clarity, those pixels with the ECT level above 10% are illustrated by empty squares with a red boundary "□."

of the simulated diagonal lines, although the pixels from the measurement are slightly scattered. Therefore, we believe that we have confirmed that those pixels observed with a high ECT level in Fig. 7 are due to higher mutual inductances contributed by the bundled long, coplanar wires.

One could simulate the effect of the mutual inductances in detail by considering the width, length, and distribution of all the coplanar wires to quantify the magnitude of the ECT in order to compare with the measurement. However, this is beyond the scope of this paper.

The high ECT for the pixels with long coplanar wires in a bundle is expected from the earlier simulation.[21] However, this is the first time experimental confirmation of this effect. To reduce this particular form of the ECT, one should introduce wires with low mutual inductances. Microstrip wires seem to be the best choice, as they are used in the LC filter chips. Furthermore, the microstrip wiring allows dense packing of many wires, making connections for more pixels feasible for a given array size. A microstrip wire is a "sandwich" structure: a superconductor on the top, a dielectric layer in the middle, and another superconductor on the bottom, while coplanar wires mean parallel superconducting wires on the top of a substrate.

Our study is also a part of the experimental demonstration of an FDM prototype for the SAFARI instrument on SPICA. Through reading out half of the array, we have established the following understanding. First, the common inductance has a negligible effect on the ECT; second, carrier leakage can cause the ECT, which depends strongly on the inter-pixel frequency spacing. In our experiment, we have shown that only adjacent pixels have a strong effect, which can cause the ECT to be 0.4%, but the remaining pixels have a negligibly low level of the ECT. The 0.4% ECT is slightly higher than the theoretical value (0.25%) due to the fact that many pixels are biased in higher than 30% of the normal resistance at the transition or have the frequency spacing smaller than 32 kHz. Although no measurement has yet been performed, with the full array connected, due to the reduction of the inter-pixel frequency spacing by a factor of 2, we expect the ECT of neighbors to reach 1.0% and the total off-resonance bias current level to be 3.2%. The total off-resonance

bias current is the quadratic summation of all off-resonance bias currents due to carrier leakage calculated using Eq. (3), as shown in Fig. 4(c). Finally, the higher mutual inductances contributed by long coplanar wires closely packed in a group can introduce a severe ECT. Therefore, the overall ECT level is dominated by the high ECT caused by mutual inductance. However, this can be mitigated by using microstrip wiring in a TES array. Furthermore, the length of the wires will become significantly shorter in practice, which also helps reduce the mutual inductance.

The latest design of the SAFARI instrument (SAFARI 4.2) requires a multiplexing factor of 120 with the same frequency span of 1 MHz–4 MHz, implying a frequency spacing of 25 kHz between pixels. Based on our current study, we expect the leakage current to dominate the ECT so that the level of the ECT of nearest neighbors is only 0.45%, while the total off-resonance bias current level will be around 1.3%. This is relatively small and is considered acceptable for the instrument.

VI. CONCLUSION AND OUTLOOK

We have developed a new method to characterize and map the ECT of an FDM system with a TES bolometer array, which is a SAFARI FDM readout prototype. By introducing a small modulation at 120 Hz in the AC bias voltage to one pixel, and measuring the response in the noise spectra of other pixels, we have for the first time mapped the ECT level of 61 pixels in an array, with a nominal frequency spacing of 32 kHz in a 61 × 61 matrix. We have found that about 94% of pixels show an ECT level of less than 0.4%. Among them, only the adjacent pixels reach that level, while the ECT level of the remaining pixels is less than 0.1%. For cases with ECT levels below 0.4%, the carrier leakage dominates the ECT. We also observe a higher ECT level, up to 10%, from the pixels that have bundled long, parallel coplanar wires. Those pixels contribute to the ECT in the 61 × 61 matrix with a unique distribution characterized by a number of parallel, diagonal lines, which match reasonably well with the hypothesis of the high mutual inductance. To mitigate the ECT due to high mutual inductances, the coplanar wires should be replaced by microstrip wires. Our study

suggests that our FDM can have a relatively low ECT level, e.g., around 0.4% if the frequency spacing is about 30 kHz. Since the base line for the SAFARI instrument is to have a frequency spacing of 25 kHz–30 kHz in the FDM readout and microstrip wiring on the detector arrays, our results promise low ECT levels in the eventual system.

In practice, all detectors are exposed to light and their carriers are modulated at the same time. We argue that our experiment reflects the right levels of electrical cross talk in practice when the detectors are exposed to very weak optical signals, which were the prime science case for SAFARI/SPICA. Since the excited modulation signals in our case are very small, we are certainly within the small signal regime and the system operates linearly. This was confirmed by applying 1%, 5%, and 10% modulation excitation and seeing that the measured ECT levels scaled with the level of excitation. This means in first order that, if multiple pixels are excited at the same time, the total cross talk signal on the other pixels will be the linear sum of the cross talk signals of those excited pixels, when excited one by one. We were not able to confirm this experimentally, since our firmware only allows for modulation of one carrier at a time but this is something that can be implemented in the future.

The study of the cross talk and non-linear effects under relatively high optical load that brings the detectors to near saturation is vital and has a major impact on calibration philosophy of the instrument. We recognize that a thorough cross talk analysis needs to address such conditions, too, but this is beyond the scope of this manuscript.

To fully characterize the crosstalk of a TES array–FDM system, one should also include an optical cross talk. In the case of the SAFARI instrument, the leak of an optical signal from one feedhorn to others in the array can cause an optical cross talk. Unlike the ECT, the optical cross talk occurs mainly in physical neighbors. To measure the optical cross talk, our setup needs to be upgraded by adding a feedhorn array in combination with an optical source, which is considered to be the next step toward a full demonstration of the SAFARI prototype.

DATA AVAILABILITY

The data that support the findings of this study are available from the corresponding author upon reasonable request.

REFERENCES

[1] D. Farrah, K. E. Smith, D. Ardila, C. M. Bradford, M. Dipirro, C. Ferkinhoff, J. Glenn, P. Goldsmith, D. Leisawitz, T. Nikola *et al.*, "Review: Far-infrared instrumentation and technological development for the next decade," J. Astron. Telesc., Instrum. Syst. **5**, 1 (2019).

[2] K. W. Christopher, *Terahertz Astronomy* (CRC Press, Boca Raton, 2016).

[3] K. D. Irwin and G. Hilton, "Transition-edge sensors," in *Cryogenic Particle Detection*, edited by C. Enss (Springer Berlin Heidelberg, Berlin, Heidelberg, 2005), pp. 63–150.

[4] Y. Zhao, Ph.D. thesis, Princeton University, 2010.

[5] D. Rigopoulou, F. Helmich, L. Hunt, J. Goicoechea, P. Hartogh, P. Fedele, M. Matsuura, L. Spinoglio, D. Elbaz, M. Griffin, G. L. Pilbratt, and E. Chapillon, "The European far-infrared space roadmap," arXiv:1701.00366 [astro-ph.IM] (2017).

[6] M. A. Dobbs, M. Lueker, K. A. Aird, A. N. Bender, B. A. Benson, L. E. Bleem, J. E. Carlstrom, C. L. Chang, H.-M. Cho, J. Clarke, T. M. Crawford, A. T. Crites, D. I. Flanigan, T. de Haan, E. M. George, N. W. Halverson, W. L. Holzapfel, J. D. Hrubes, B. R. Johnson, J. Joseph, R. Keisler, J. Kennedy, Z. Kermish, T. M. Lanting, A. T. Lee, E. M. Leitch, D. Luong-Van, J. J. McMahon, J. Mehl, S. S. Meyer, T. E. Montroy, S. Padin, T. Plagge, C. Pryke, P. L. Richards, J. E. Ruhl, K. K. Schaffer, D. Schwan, E. Shirokoff, H. G. Spieler, Z. Staniszewski, A. A. Stark, K. Vanderlinde, J. D. Vieira, C. Vu, B. Westbrook, and R. Williamson, "Frequency multiplexed superconducting quantum interference device readout of large bolometer arrays for cosmic microwave background measurements," Rev. Sci. Instrum. **83**, 073113 (2012).

[7] W. B. Doriese, J. A. Beall, S. Deiker, W. D. Duncan, L. Ferreira, G. C. Hilton, K. D. Irwin, C. D. Reintsema, J. N. Ullom, L. R. Vale, and Y. Xu, "Time-division multiplexing of high-resolution x-ray microcalorimeters: Four pixels and beyond," Appl. Phys. Lett. **85**, 4762–4764 (2004).

[8] D. Prêle, F. Voisin, M. Piat, T. Decourcelle, C. Perbost, C. Chapron, D. Rambaud, S. Maestre, W. Marty, and L. Montier, "A 128 multiplexing factor time-domain SQUID multiplexer," J. Low Temp. Phys. **184**, 363–368 (2016).

[9] B. D. Jackson, P. A. J. de Korte, J. van der Kuur, P. D. Mauskopf, J. Beyer, M. P. Bruijn, A. Cros, J. Gao, D. Griffin, R. den Hartog, M. Kiviranta, G. de Lange, B. van Leeuwen, C. Macculi, L. Ravera, N. Trappe, H. van Weers, and S. Withington, "The SPICA-SAFARI detector system: TES detector arrays with frequency-division multiplexed SQUID readout," IEEE Trans. Terahertz Sci. Technol. **2**, 12–21 (2012).

[10] D. Schwan, P. A. R. Ade, K. Basu, A. N. Bender, F. Bertoldi, H.-M. Cho, G. Chon, J. Clarke, M. Dobbs, D. Ferrusca *et al.*, "Invited Article: Millimeter-wave bolometer array receiver for the Atacama pathfinder experiment Sunyaev-Zel'dovich (APEX-SZ) instrument," Rev. Sci. Instrum. **82**, 091301 (2011).

[11] J. S. Avva, P. A. R. Ade, Z. Ahmed *et al.*, "Particle physics with the cosmic microwave background with SPT-3G," arXiv:1911.08047 [astro-ph.CO] (2019).

[12] H. Logan, Ph.D. thesis, University of California, San Diego, 2019.

[13] G. Signorelli, A. M. Baldini, C. Bemporad, M. Biasotti, F. Cei, V. Ceriale, D. Corsini, F. Fontanelli, L. Galli, G. Gallucci, F. Gatti, M. Incagli, M. Grassi, D. Nicolò, F. Spinella, D. Vaccaro, and M. Venturini, "A 16 channel frequency-domain-modulation readout system with custom superconducting LC filters for the SWIPE instrument of the balloon-borne LSPE experiment," Nucl. Instrum. Methods Phys. Res., Sect. A **824**, 184–186 (2016).

[14] A. Tartari, A. M. Baldini, F. Cei, L. Galli, M. Grassi, D. Nicolò, M. Piendibene, F. Spinella, D. Vaccaro, and G. Signorelli, "Development and testing of the FDM read-out of the TES arrays aboard the LSPE/SWIPE balloon-borne experiment," J. Low Temp. Phys. **199**, 212–218 (2020).

[15] P. R. Roelfsema, H. Shibai, L. Armus, D. Arrazola, M. Audard, M. D. Audley, C. Bradford, I. Charles, P. Dieleman, Y. Doi *et al.*, *SPICA—A Large Cryogenic Infrared Space Telescope: Unveiling the Obscured Universe* (Publications of the Astronomical Society of Australia, 2018), Vol. 35.

[16] G. de Lange, P. Roelfsema, M. Giard, F. Najarro, K. Wafelbakker, W. Jellema, B. Jackson, M. Audard, M. Griffin, F. Kerschbaum, D. Naylor, A. Poglitsch, M. Bradford, and B. Vandenbussche, *The SAFARI Grating Spectrometer for the SPICA Space Observatory* (SPIE, 2018).

[17]D. Barret, J. W. den Herder, L. Piro *et al.*, "The hot and energetic Universe: The X-ray integral field unit (X-IFU) for Athena+," arXiv:1308.6784 [astro-ph.IM] (2013).

[18]L. Gottardi, H. Akamatsu, D. Barret, M. P. Bruijn, R. H. den Hartog, J. den Herder, H. F. C. Hoevers, M. Kiviranta, J. van der Kuur, A. J. van der Linden *et al.*, "Development of TES-based detectors array for the X-ray Integral Field Unit (X-IFU) on the future x-ray observatory ATHENA," in *Space Telescopes and Instrumentation 2014: Ultraviolet to Gamma Ray* (SPIE, 2014), Vol. 9144, pp. 792–798.

[19]G. C. Jaehnig, K. Arnold, J. Austermann, D. Becker, S. Duff, N. W. Halverson, M. Hazumi, G. Hilton, J. Hubmayr, A. T. Lee, M. Link, A. Suzuki, M. Vissers, S. Walker, and B. Westbrook, "Development of space-optimized TES bolometer arrays for LiteBIRD," J. Low Temp. Phys. **199**, 646 (2020).

[20]R. den Hartog, C. Kirsch, C. de Vries, H. Akamatsu, T. Dauser, P. Peille, E. Cucchetti, B. Jackson, S. Bandler, S. Smith, and J. Wilms, "Crosstalk in an FDM laboratory setup and the athena X-IFU end-to-end simulator," J. Low Temp. Phys. **193**, 533–538 (2018).

[21]X. Yan, M. P. Bruijn, H. J. van Weers, R. A. Hijmering, J. van der Kuur, and J. R. Gao, "Modeling inductances of wiring for a TES array read by FDM," IEEE Trans. Appl. Supercond. **25**, 1–5 (2015).

[22]M. P. Bruijn, L. Gottardi, R. H. Hartog, J. van der Kuur, A. J. van der Linden, and B. D. Jackson, "Tailoring the high-Q LC filter arrays for readout of kilo-pixel TES arrays in the SPICA-SAFARI instrument," J. Low Temp. Phys. **176**, 421–425 (2014).

[23]K. Sakai, Y. Takei, R. Yamamoto, N. Y. Yamasaki, K. Mitsuda, M. Hidaka, S. Nagasawa, S. Kohjiro, and T. Miyazaki, "Baseband feedback frequency-division multiplexing with low-power dc-SQUIDs and digital electronics for TES X-ray microcalorimeters," J. Low Temp. Phys. **176**, 400–407 (2014).

[24]R. A. Hijmering, R. den Hartog, M. L. Ridder, A. J. van der Linden, J. van der Kuur, J. R. Gao, and B. Jackson, *Readout of a 176 Pixel FDM System for SAFARI TES Arrays* (SPIE, 2016), pp. 321–333, note we used the same TES array as described in this paper, but the correct thickness of Si_3N_4 should be 0.25 μm.

[25]Janis Products, https://www.janis.com/products/janis-products, 2020.

[26]T. Suzuki, P. Khosropanah, M. L. Ridder, R. A. Hijmering, J. R. Gao, H. Akamatsu, L. Gottardi, J. van der Kuur, and B. D. Jackson, "Development of ultra-low-noise TES bolometer arrays," J. Low Temp. Phys. **184**, 52–59 (2016).

[27]M. D. Audley, Q. Wang, R. A. Hijmering, P. Khosropanah, G. de Lange, A. J. van der Linden, M. L. Ridder, and E. Taralli, "SQUID noise in a 176-pixel FDM demonstrator for the SAFARI far-infrared spectrometer," J. Low Temp. Phys. **199**, 723–729 (2020).

[28]Q. Wang, M. D. Audley, P. Khosropanah, J. van der Kuur, G. de Lange, A. Aminaei, D. Boersma, F. van der Tak, and J.-R. Gao, "Noise measurements of a low-noise amplifier in the FDM readout system for SAFARI," J. Low Temp. Phys. **199**, 817–823 (2020).

[29]J. van der Kuur, P. A. J. de Korte, P. de Groene, N. H. R. Baars, M. P. Lubbers, and M. Kiviranta, "Implementation of frequency domain multiplexing in imaging arrays of microcalorimeters," Nucl. Instrum. Methods Phys. Res., Sect. A **520**, 551–554 (2004).

[30]E. Taralli, P. Khosropanah, L. Gottardi, K. Nagayoshi, M. L. Ridder, M. P. Bruijn, and J. R. Gao, "Complex impedance of TESs under AC bias using FDM readout system," AIP Adv. **9**, 045324 (2019).